ENGINEERING

Limpet teeth microstructure unites auxeticity with extreme strength and high stiffness

Sang Ho Oh[1,2]*†, Jin-Kyung Kim[1,3]†, Yue Liu[4,5]†, Michael Wurmshuber[6], Xiang-Long Peng[7,8], Jinsol Seo[1,2], Jiwon Jeong[1], Zhen Wang[1], Jana Wilmers[7], Celal Soyarslan[7,9,10], Jongil Kim[1,2], Boonsita Kittiwirayanon[1], Jeehun Jeong[1,2], Hyo-Jeong Kim[11], Yang Hoon Huh[11], Daniel Kiener[6], Swantje Bargmann[7,12], Huajian Gao[4,13,14]*

Materials displaying negative Poisson's ratio, referred to as auxeticity, have been found in nature and created in engineering through various structural mechanisms. However, uniting auxeticity with high strength and high stiffness has been challenging. Here, combining in situ nanomechanical testing with microstructure-based modeling, we show that the leading part of limpet teeth successfully achieves this combination of properties through a unique microstructure consisting of an amorphous hydrated silica matrix embedded with bundles of single-crystal iron oxide hydroxide nanorods arranged in a pseudo-cholesteric pattern. During deformation, this microstructure allows local coordinated displacement and rotation of the nanorods, enabling auxetic behavior while maintaining one of the highest strengths among natural materials. These findings lay a foundation for designing biomimetic auxetic materials with extreme strength and high stiffness.

INTRODUCTION

Biological structural materials usually comprise mineralized hard and nonmineralized soft structures arranged in complex hierarchical architectures (*1*–*3*), often achieving orders-of-magnitude increases in strength and toughness above those of their constituents (*4*, *5*), and exhibit characteristics of multifunctionality and multiscale structure-property relationships (*1*, *4*). Auxetic biological materials with a negative Poisson's ratio have attracted considerable attention because of their superior mechanical properties, such as enhanced shear resistance, indentation resistance, and fracture toughness, which can often be associated with the primary functions of such materials. While various microstructural features giving rise to auxeticity have been found in nature, e.g., cancellous bone (*6*), human tendon (*7*), cat skin (*8*), cow teat skin (*9*), nacre (*10*), and spider silk (*11*), and created in engineering through various structural mechanisms, e.g., nonaffine deformation, non–central force interaction, and chiral structures (*12*–*16*), a microstructure that unites auxeticity with both high strength and high stiffness is extremely rare.

Limpet teeth have evolved to withstand contact with rocks, as the limpet's feeding mechanism requires rasping the teeth over rock surfaces without catastrophic failure (*17*–*20*). They have been reported as the strongest natural material, with tensile strengths ranging from 3.0 to 6.5 GPa (*19*), thereby outperforming spider silk (*21*). The limpet tooth was suggested as an ideal natural composite with optimized stress transfer between matrix and reinforcing nanorods (*18*, *19*). The present work reports that the leading part of mature limpet teeth exhibits a microstructure that unites auxeticity with ultrahigh strength and high stiffness. The micromechanical mechanisms governing the auxetic behavior are investigated using a combined approach of in situ transmission electron microscopy (TEM)–based nanomechanical testing and finite element modeling (FEM). The pseudo-cholesteric pattern of the nanorods and their strong cohesion with the matrix through unique structural and chemical optimization facilitate nanorod displacement and rotation as well as optimal stress transfer, leading to auxetic behavior while maintaining one of the highest strengths among natural materials.

RESULTS

Mature, fully mineralized teeth of limpet are composed of iron oxide hydroxide (α-FeOOH, goethite, space group *Pbnm*) crystal nanorods embedded in an amorphous hydrated silica (SiO_2•nH_2O) matrix (*22*, *23*) (Fig. 1). Scanning TEM (STEM) energy-dispersive x-ray spectroscopy (EDS) and electron energy-loss spectroscopy (EELS) analyses (fig. S1) showed that the nanorods consist of Fe and O, while the matrix is made of Si and O. As revealed by electron microscopy characterization, limpet teeth have a functionally graded microstructure, which evidently spans from the leading to the trailing part (fig. S2) to optimize the respective mechanical performance. In the leading part, the nanorods have an average diameter of 32.1 ± 0.4 nm and an average length of 279.0 ± 18.4 nm, with a volume fraction of 51.5 ± 1.8% (fig. S3). They are arranged in a pseudo-cholesteric pattern (*22*), where predominantly horizontally aligned nanorods weave around vertically aligned nanorod bundles (Fig. 1C). The three-dimensional (3D) microstructure reconstructed by TEM tilt-series tomography confirmed the vertical nanorods to be of the same kind as the horizontal ones (Fig. 1D, fig. S4, and movies S1 and S2). The

[1]Department of Energy Science, Sungkyunkwan University, Suwon, Korea. [2]Department of Energy Engineering, Korea Institute of Energy Technology (KENTECH), Naju, Korea. [3]Department of Material Science and Chemical Engineering, Hanyang University, Ansan, Korea. [4]School of Engineering, Brown University, Providence, RI 02912, USA. [5]Department of Mechanical Engineering, University of Michigan, Ann Arbor, MI 48109, USA. [6]Department of Materials Science, Chair of Materials Physics, Montanuniversität Leoben, Leoben, Austria. [7]Chair of Solid Mechanics, University of Wuppertal, Wuppertal, Germany. [8]Mechanics of Functional Materials Division, Institute of Materials Science, Technische Universität Darmstadt, Darmstadt 64287, Germany. [9]Chair of Nonlinear Solid Mechanics, Faculty of Engineering Technology, University of Twente, Enschede 7522 NB, Netherlands. [10]Fraunhofer Innovation Platform, University of Twente, Enschede 7522 NB, Netherlands. [11]Electron Microscopy Research Center, Korea Basic Science Institute, Cheongju, Korea. [12]Wuppertal Center for Smart Materials and Systems, University of Wuppertal, Wuppertal, Germany. [13]School of Mechanical and Aerospace Engineering, College of Engineering, Nanyang Technological University, 70 Nanyang Drive, Singapore 639798, Singapore. [14]Institute of High Performance Computing, A*STAR, Singapore 138632, Singapore.
*Corresponding author. Email: shoh@kentech.ac.kr (S.H.O.); huajian.gao@ntu.edu.sg (H.G.)
†These authors contributed equally to this work.

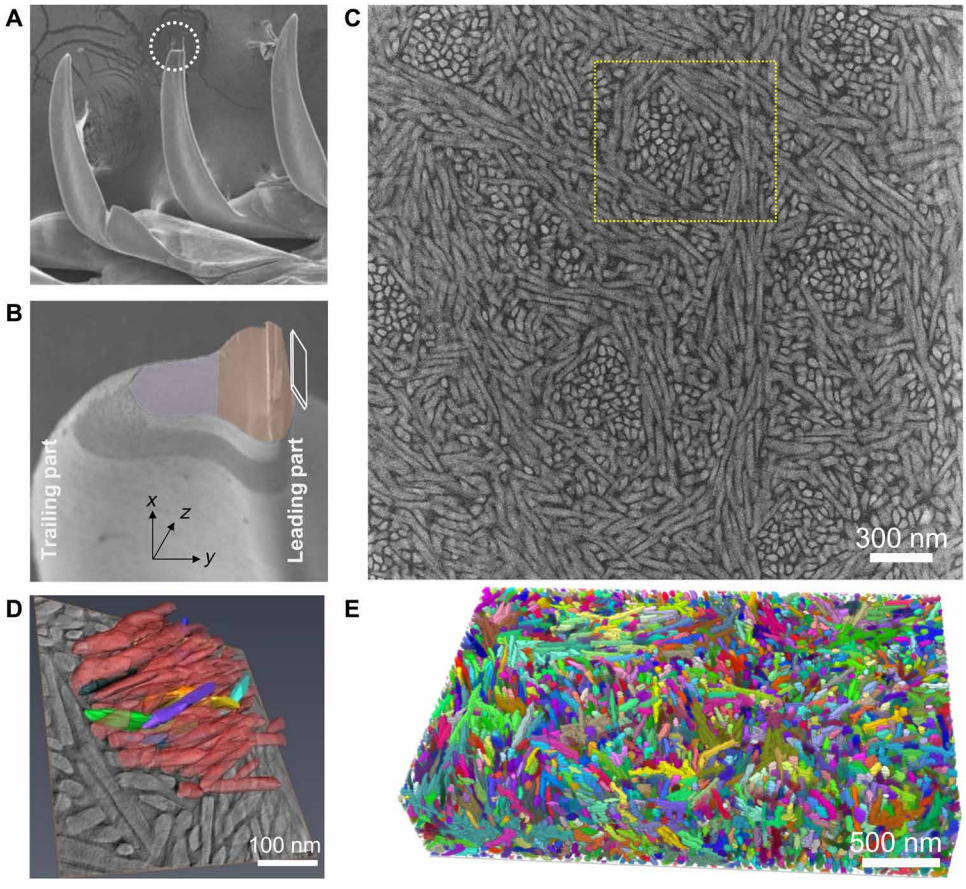

Fig. 1. Microstructure of the leading part of a limpet tooth. (**A**) SEM overview image of mature limpet teeth. The tip of the tooth where TEM samples were prepared from is indicated by a white dotted circle. (**B**) SEM image of a FIB cross-sectioned tooth. The side facing the direction of scraping is referred to as the leading part and the opposite side as the trailing part. TEM sample prepared from the leading part is illustrated schematically. (**C**) STEM HAADF image showing the internal microstructure of the leading part. The goethite (α-FeOOH) nanorods appear bright in the amorphous hydrated silica (SiO_2•nH_2O) matrix. Bundles of vertical nanorods are enveloped by horizontally aligned ones in a pseudo-cholesteric pattern. (**D**) 3D morphology of a vertical nanorod bundle reconstructed by TEM tilt-series tomography (refer to movies S1 and S2). The particle-shaped crystals surrounded by horizontally aligned nanorods in (C) correspond to cross sections of vertical nanorods of the same kind. Vertically aligned nanorods are shown in red and others in various colors. (**E**) 3D microstructure of the leading part over a larger area containing several vertical nanorod bundles (refer to movie S3) The 3D microstructure reconstructed obtained from a series of FIB serial sectioning SEM images was used for FEM. All colors in (D) and (E) are artificially introduced for better visualization.

bundle diameter is ~0.5 to 1 μm, while the average spacing is ~1 μm. The large-area 3D microstructure containing several vertical nanorod bundles, reconstructed from a set of focused ion beam (FIB) serial-sectioned scanning electron microscopy (SEM) images, revealed a complex pseudo-cholesteric pattern of the horizontal nanorods surrounding the vertical nanorod bundles (Fig. 1E and movie S3).

The nanorods in the leading part are composed of single-crystalline goethite without structural defects, pores, or cracks (Fig. 2A). The goethite nanorods all have their long axes aligned parallel to the [001] direction. The perfect single crystallinity and small size of the nanorods could play a decisive role in nanostructural optimization to ensure optimum strength and maximum tolerance of flaws (*24*). The goethite nanorods are encapsulated by an interfacial phase with a thickness of a few nanometers (yellow dashed lines in Fig. 2, A and C), featuring a similar chemical composition but different atomic structure compared to the goethite, constituting a core/shell structure. On the basis of the STEM high-angle annular dark-field (HAADF) image simulation and comparison of EELS results of the O-K and Fe-$L_{2,3}$ edges with reference spectra (*25*), the interface phase is identified as magnetite (Fe_3O_4) (fig. S5). Besides, a transition zone exists on the matrix side of the interface, where the chemical composition changes gradually over ~3 nm (red arrow in Fig. 2, B and C). This uniquely graded interface can play an essential role in efficient stress transfer between the stiff nanorods and the soft matrix and in facilitating the rotation of the nanorods while maintaining strong adhesion during deformation.

Site-specific mechanical tests of limpet teeth were performed via in situ micropillar compression (fig. S6 and movies S4 and S5) to determine the local mechanical properties. For the micropillar compression, multiple pillars were prepared in both trailing and leading parts of the tooth cross section by FIB (fig. S6B) and tested using a flat diamond punch. None of them exhibit noticeable plasticity; rather, they deform elastically until fracture (fig. S6C). The ultimate compressive failure strength and elastic modulus of the leading part are 3.59 ± 0.29 and 38.4 ± 6.2 GPa, respectively. Because of the combination of high strength and relatively low modulus, an extensive elastic regime is observed in the stress-strain curves (fig. S6C). Notably, the determined failure strength and modulus are notably

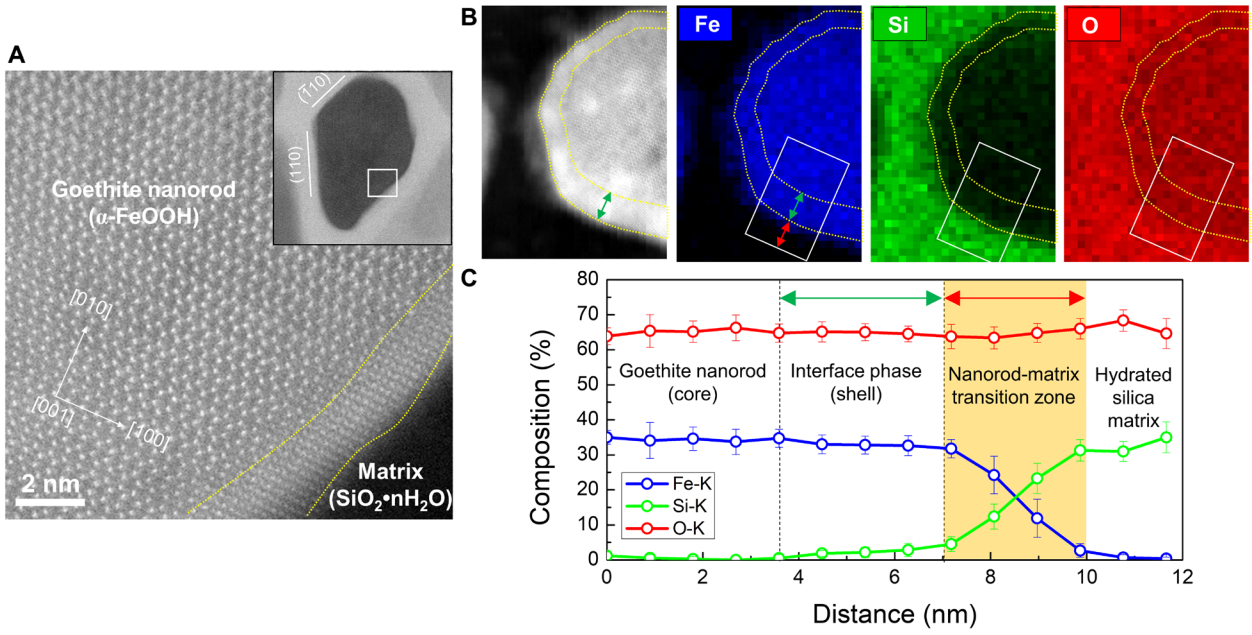

Fig. 2. Structure and chemical composition of the goethite nanorod. (**A**) Atomic-resolution STEM HAADF image showing a few-nanometer-thick interface phase (outlined by yellow dotted lines) present at the interface between the nanorod and matrix. The interface phase surrounding the internal goethite part of the nanorod has a similar chemical composition but different atomic structure (refer to fig. S5). (**B**) STEM HAADF image and EELS elemental maps of a vertical nanorod obtained by quantification of O-K, Si-$L_{2,3}$, and Fe-$L_{2,3}$ edges. (**C**) EELS line profiles obtained from the white box drawn in the EELS elemental maps in (B). The approximately 3 nanometer-thick interface phase (green arrow) encapsulating the nanorod has a similar chemical composition to that of the goethite, but with a different atomic structure, constituting a core/shell structure. The composition change from the shell region of the nanorod to the matrix occurs gradually over ~3 nm, indicating the existence of a chemical transition zone (red arrow) between the nanorod and matrix. Considering the STEM probe of 0.14 nm in diameter, the observed composition profile is unlikely induced by beam broadening.

lower than the tensile strength of 4.90 GPa and elastic modulus of 120 GPa reported by Barber *et al.* (*19*). The differences may be most likely attributed to the much smaller volume tested by Barber *et al.* (*19*), who essentially probed aligned fiber bundles. In contrast, tens of thousands of fibers are loaded in the present case, ensuring sampling of a representative bulk behavior. Consequently, our larger samples contain increased fractions of off-axis oriented reinforcement fibers, resulting in lower strength and modulus.

To reveal the auxetic deformation mechanism at the microstructural level, we carried out in situ STEM tensile testing (Fig. 3 and figs. S7 to S9). Low-magnification STEM images of a limpet tooth recorded at different displacements (Fig. 3A) were used to assess the geometrical changes of tensile samples along the transverse and the longitudinal directions. Figure 3B shows the measured longitudinal and transverse strain, as well as the resultant Poisson's ratio, for samples with loading axis *z* (samples A, B, and C) and axis *x* (sample D), respectively. The strain measured at different locations (top) is color-coded accordingly. The averaged longitudinal and transverse strains (middle) from a total of four measurements show a clear negative Poisson's ratio over a wide range of strain (bottom). The Poisson's ratio increases gradually with strain and approaches zero at about 2% longitudinal strain. These results clearly demonstrate the existence of auxeticity at the microstructural level of the limpet teeth.

Auxeticity is a linear elastic behavior and therefore does not depend on tension or compression. Therefore, both compression and tension tests can be used to probe the Poisson's ratio at different strain levels. Nonetheless, the two methods complement each other with their respective advantages and limitations. In situ TEM tensile straining has advantages in accurate measurements of strains and thus Poisson's ratio, owing to the good image resolution (small pixel size). However, the mechanical properties cannot be measured quantitatively as the TEM straining holder was not equipped with a force sensor. On the other hand, the mechanical properties can be measured via the built-in nanoindentation system in SEM microcompression. However, because of the large pixel size of the SEM image (18.5 nm per pixel), the smallest measurable strain allowing the determination of Poisson's ratio in SEM microcompression is limited to ~2% (fig. S6, G and H), which corresponds roughly to the failure strain in TEM experiments at which the Poisson's ratio approaches zero (Fig. 3B). This pixel size limits, in particular, strain resolution in the transverse direction, causing the large scatter of measured Poisson's ratio around zero (fig. S10). Given such limitations, the SEM image–based strain analysis is not suitable for capturing the auxetic response of limpet teeth, which occurs at the low-strain regime. On the other hand, the wide range of compressive strain (up to the ultimate failure strain of ~10%) makes SEM microcompression tests ideally suited for the measurement of failure strength and stiffness of this strong yet brittle composite material. Combining the two methods, we can access the whole strain regime from pronounced auxeticity at low strains toward diminishing Poisson ratios for strains exceeding ~2% up to the compressive failure strain of ~10%.

The analysis of in situ TEM images reveals a typical spin pattern in vertically aligned nanorod bundles and concurrent rotation of individual nanorods therein, suggesting that the observed auxeticity is likely associated with the localized rotation of the microstructure (Fig. 4). Figure 4A details one of the spin patterns by displaying the

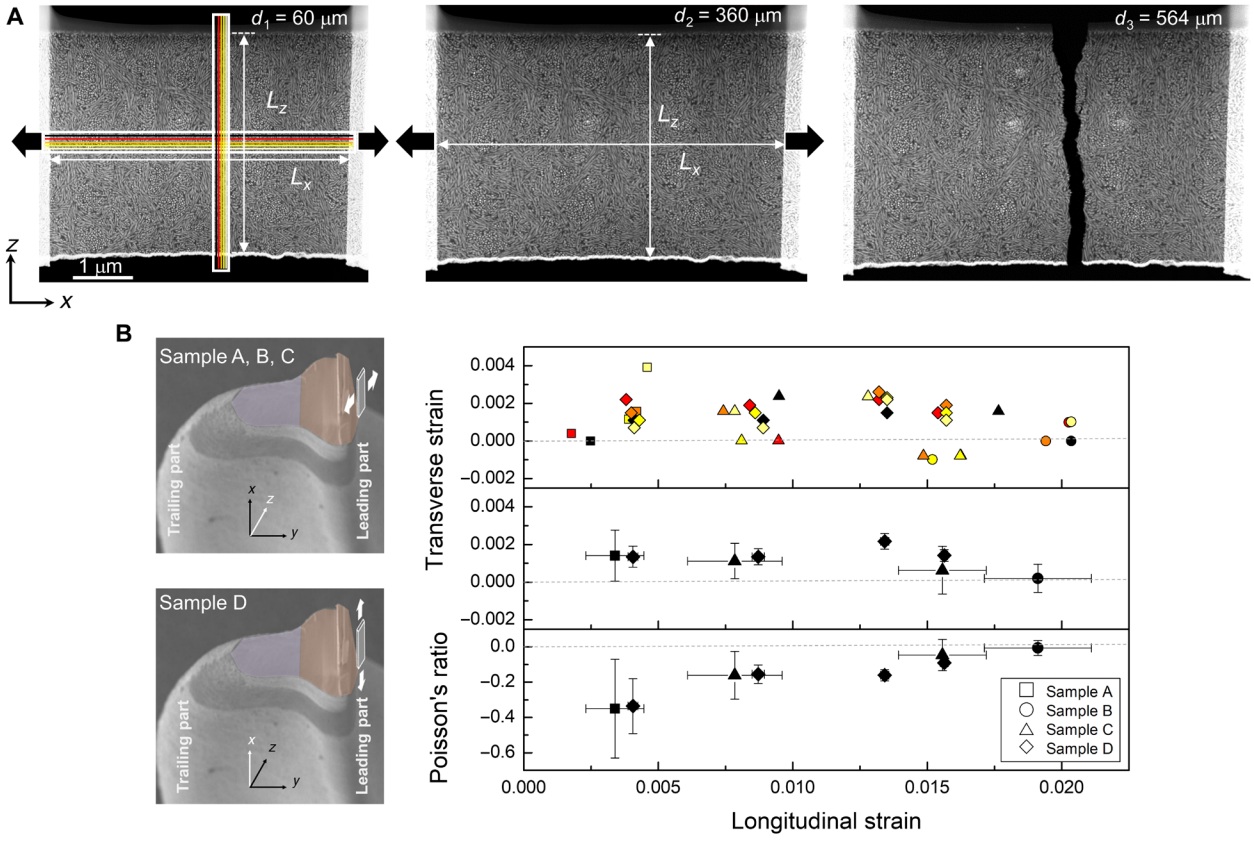

Fig. 3. Direct measurement of Poisson's ratio using TEM images obtained in the course of in situ tensile tests. (**A**) TEM images of limpet tooth recorded at different displacements (d_i). Longitudinal strain is measured by the change of the gauge length ($L_{z,i}$) along the tensile axis and transverse strain from the change in width ($L_{x,i}$) of the central region of the tensile sample along the transverse direction. The measurement window (white-lined box) for transverse strain is chosen as the region where the crack is generated by referring to the fractured sample. As illustrated by differently colored lines in the measurement window, in total, five measurements have been conducted for each TEM image by shifting the 12-pixel-wide sampling area by 6 pixels (fig. S8). The same methodology was applied to four different TEM experiments (fig. S9). (**B**) The measured longitudinal and transverse strain, as well as the resultant Poisson's ratio for samples with loading axis *z* (samples A, B, and C) and loading axis *x* (sample D), respectively. The transverse strain measured at different locations (top) is color-coded accordingly. The averaged longitudinal and transverse strains (middle) from four measurements show a clear negative Poisson's ratio over a wide range of strain (bottom). The Poisson's ratio increases gradually with strain and approaches zero at about 2% longitudinal strain.

displacement vector of each vertical nanorod in a bundle for two superimposed TEM images recorded at different strain. The displacement vectors (indicated by red arrows) were determined by tracking the positions of individual nanorods. The displacement vector map (ω_R) visualizes the collective and coordinated displacement of vertical nanorods, showing a revolving spin pattern where the displacement magnitude increases with the distance from the bundle center. The vertical nanorod bundles can be generally associated with local peaks or valleys of the spin field (fig. S11).

A detailed digital image correlation (DIC) analysis performed on individual nanorods in a revolving spin pattern region revealed the rotation of nanorods around their axis during deformation (Fig. 4B and fig. S12). The rotation angle (ϕ_R) was measured by rotating the displaced nanorod in increments of 0.1° until its edge perfectly coincides with the original orientation (fig. S13). This DIC analysis showed that a group of nanorods in the bundle rotates predominantly counterclockwise (+ in sign convention and red in binary color scale) and others clockwise (− sign and green color), with the rotation angle increasing with the distance from the bundle center, reaching a maximum of ±7° to 8°, respectively. We hypothesize that the two rotation modes, i.e., the revolving spin pattern arising from the collective and coordinated displacement of vertical nanorods and their simultaneous on-axis rotation, are the primary microstructural origin enabling the auxeticity of the limpet tooth.

We consider the elastic anisotropy of the goethite crystal as a possible factor influencing the rotation of nanorods. Geometrical phase analysis (GPA) of high-resolution TEM (HRTEM) images of several nanorods at different displacements showed that tensile strain is induced predominantly along the [100] direction, but compressive strain emerges along the [010] direction of nanorods, independent of the loading direction (Fig. 4C and figs. S14 to S16). As verified by density functional theory calculation, the [100] direction has been identified as the most compliant axis of the goethite crystal (fig. S17), and its alignment toward the loading direction leads to reduced elastic energy.

The evolution of specific rotation fields within a revolving spin pattern depends on the internal microstructure, such as the crystallographic orientation and shape of nanorods, and their arrangement within the bundle. Figure 4C shows that the cross section of vertical nanorods is irregular but close to a rounded rhomboid with the

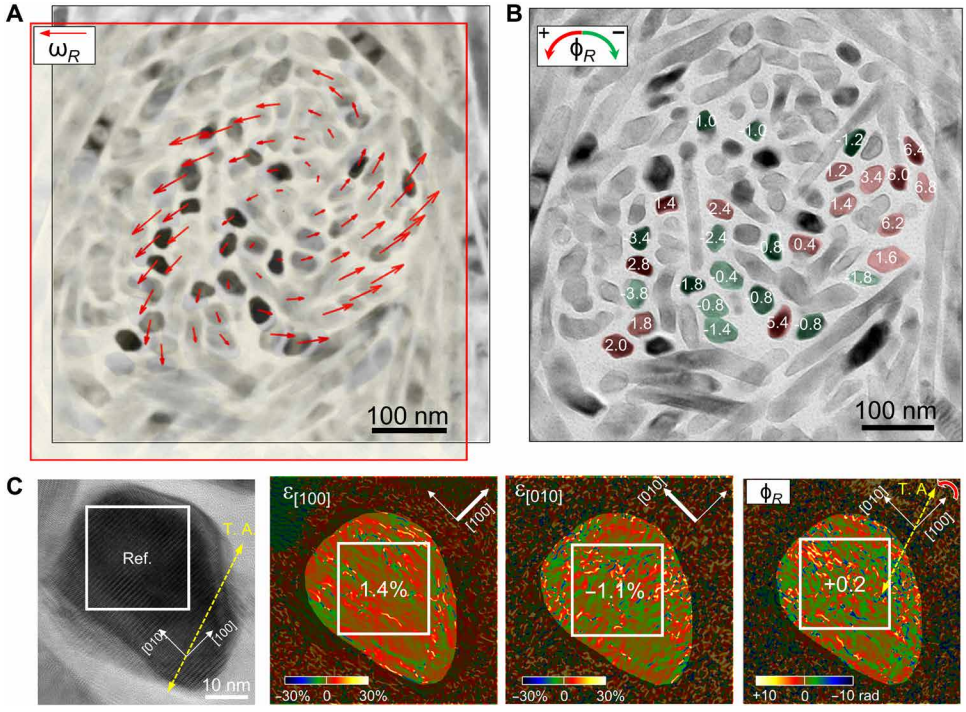

Fig. 4. Quantitative analysis of in situ TEM data showing nanorod displacement and rotation. (**A**) Displacement vector map of vertical nanorods in a bundle, showing a revolving spin pattern. The displacement vectors (multiplied by 1.5 for visibility) are overlaid. (**B**) Rotation of individual vertical nanorods around their axis. The number indicates the rotation angle in degree, while the color indicates the rotation direction. (**C**) In situ HRTEM image, GPA strain, and rotation map of a vertical nanorod, showing tensile strain along the [100] and compressive strain along the [010] direction (refer to figs. S16 and S17), resulting in a counterclockwise rotation. The tensile axis (T.A.) is indicated by a yellow dashed arrow.

facets along the {110} planes (Fig. 2A), where the [100] and [010] directions are oriented along the short and long diagonal, respectively (Fig. 4C and figs. S15 and S16). The rotation direction is determined by the relative orientation of the compliant [100] direction with respect to the loading direction, and specific rotation fields are coordinated to minimize the strain energy.

Auxetic behavior was observed only in the longitudinal section of the leading part, where vertical nanorod bundles are embedded in a sea of horizontally aligned nanorods, but not in other orthogonal sections of the leading part or in any sections of the trailing part (figs. S18 and S19). In addition, the small region containing a vertical bundle showed stronger spin than its surroundings and a larger negative Poisson's ratio than the entire region, further suggesting the significance of the local microstructure (fig. S20). These observations also underline that the collective and cooperative rotation of the nanorods becomes inactive when the deformation turns to typical nonauxetic behavior with positive Poisson's ratio at a larger strain close to failure (fig. S20C). As the nanorods rotate and align with the loading direction with straining, the external strain will be gradually undertaken by direct stretching of nanorods, which thus deactivate the rotation-based mechanism. The observed transition in rotation pattern (fig. S20, B and C) indicates that a high strain can deactivate the rotation mechanism that leads to auxeticity and thus explains why Poisson's ratio increases with the loading (Fig. 3B).

The presence of a nanometer-thick interface phase and transition zone with a composition gradient across the rod-matrix interface ensures strong nanorod-matrix cohesion and efficient stress transfer between neighboring nanorods within a bundle, allowing coordinated displacement. Such coordinated displacements result in a distinct spin pattern, and the system effectively resembles a chiral lattice. The uniquely graded rod-matrix interface is expected to alleviate interfacial stresses by avoiding a sharp modulus and strength mismatch between the rod and matrix (*26*) and to inhibit delamination while allowing microstructural rotation. No interface delamination has been observed throughout the in situ TEM tensile straining experiments (movie S6). Furthermore, the strong nanorod-matrix cohesion prevents the development of large shear stresses/strains during rotation, which could induce interfacial fracture/sliding. In situ TEM tensile straining shows a crack propagating through both the matrix and the nanorods, rather than along the interfaces, which suggests an extraordinarily strong interfacial fracture resistance (fig. S21A and movie S7). Furthermore, the crack seems to deflect from the vertical nanorod bundles, suggesting structural crack deflection as a toughening mechanism operative in these regions (fig. S21B).

The nanometer-thick compositionally graded intermediate layer present at the rod-matrix interface could improve rod/matrix adhesion and mechanical load transfer (*27*). A similar graded interface was also reported for chiton teeth (*28*). On the other hand, a theoretical study showed that decreasing the dimension of the mineral led to an increase in the interface strength (*29*). The nanorods observed in the present work are small enough to ensure optimum strength and maximum tolerance of flaws. Thus, the combined effect of the graded interface and the small dimension of the rods could contribute to the expected high strength of the rod-matrix interface. Barber *et al.* (*19*) reported a progressive failure of the nanorods upon tensile tests of limpet tooth samples. The fragmentation of the nanorods could indicate

that the stress transfer at the rod-matrix interface is strong enough to fracture the nanorods. This is in sharp contrast to interfacial failure and pullout of the mineral phase observed for nacre (*30*).

To further confirm that the microstructure rotation plays an essential role in the observed auxetic behavior of the material, we performed detailed FEM analyses (fig. S6C) based on the 3D microstructures generated from FIB serial sectioning images (Fig. 1E and fig. S4, C and D). While the FEM correctly predicted the elastic stiffness of the material, it failed to capture the auxetic behavior as it does not explicitly account for microstructural rotation. Thus, to computationally investigate possible microstructural mechanisms responsible for a negative Poisson's ratio, we construct a structural unit cell model that takes the elastic anisotropy of the nanorod-matrix composite into account and characterize it using micropolar elasticity theory (Fig. 5A). In the unit cell, the rod-matrix composite was homogenized as a transversely isotropic material (Fig. 5B and fig. S22A) with the longitudinal modulus $E_{//}$ (along the rod) and transverse modulus $E_{\perp}$ (perpendicular to the rod) using the Mori-Tanaka theory (*31*, *32*), which requires inputs of the rod volume fraction, aspect ratio, and elastic constants of the rod and matrix, respectively. In the six adjacent "arm" domains, a spiral-like in-plane orientation pattern mimics the horizontal bundles. The center node with an out-of-plane material orientation corresponds to the vertical bundle (Fig. 5A). Such a unit cell can be further homogenized into a micropolar continuum (Fig. 5, C and D). Strain energy can be induced by the difference between the average rotation ϕ in the center node, corresponding to the microstructure rotation in micropolar elasticity, and the average spin ω of the entire unit cell, corresponding to the continuum displacement-induced spin (Fig. 5E, fig. S22B, and movie S8). The average rotation ϕ defined in the simulation originated from the revolving spin pattern generated by the collective displacement of the individual vertical nanorods (ω_R) measured in the DIC analysis (Fig. 4A).

We characterize the 2D micropolar elastic constant A along with its Lamé constants λ and μ and plane-stress Poisson's ratio ν. The Poisson's ratio values obtained through different effective nanorod aspect ratios and relative nanorod moduli E_{rod}/E_{mat} all follow the same master curve governed by $E_{//}/E_{\perp}$ (fig. S23), which is identified as the sole control material parameter. Auxeticity is observed for an E_{rod}/E_{mat} value larger than ~10^2, which is comparable to the order of magnitude of the modulus ratio between goethite and hydrated silica (*33*). Furthermore, an increasing modulus anisotropy ratio $E_{//}/E_{\perp}$ produces a lower Poisson's ratio (Fig. 5F). Besides, for a given r/L, the magnitude of micropolarity, defined as $|A|/(\lambda+\mu)$, increases with decreasing Poisson's ratio (Fig. 5, F and G). Inside the auxetic regime (enclosed by the black dashed lines in Fig. 5, F and G), the magnitude of $|A|/(\lambda+\mu)$ is non-negligible, which confirms the importance of using micropolar elasticity to characterize such structures instead of conventional linear elasticity. Maximum auxeticity is predicted around $r/L = 0.3$, where auxeticity occupies the largest parameter regime (Fig. 5F), comparing reasonably well to the value $r/L = 0.41$ of the area occupied by vertical bundles inside the colored region in fig. S11. These observations imply that micropolar elasticity can provide a viable description for the deformation mechanism and the auxeticity of the limpet teeth microstructure.

We also wish to point out that, although the 2D micropolar modeling was able to capture the experimentally observed auxetic behavior, it is currently not clear how to extend it to 3D based on the actual limpet microstructure. As a composite material, the strength and modulus of the limpet teeth depend primarily on the parameters that characterize the composite model, such as volume fraction, shape/size, and spatial arrangement of nanorods. As we demonstrated, these parameters are secured well by various TEM and FIB imaging and related image analysis and yield reasonable modulus prediction (fig. S6C). However, there is currently no appropriate theoretical framework that is capable of producing a complete description of the microstructure and mechanical properties of limpet teeth down to the length scales where the core/shell structure of nanorods and nanorod/matrix interface are relevant. A full 3D modeling of the limpet microstructure is currently beyond the state-of-the-art theoretical and computational capabilities. We were nevertheless able to clearly observe auxetic behavior in the 2D micropolar modeling by allowing the unit cell for not only displacement but also the rotation, as observed in our TEM analysis, which thus confirms the critical importance of the nanorod rotation in the observed auxetic behavior.

DISCUSSION

In summary, we report a combination of negative Poisson's ratio, extreme strength, and high stiffness associated with the microstructure in the leading part of the limpet tooth, which consists of an amorphous hydrated silica matrix embedded with bundles of goethite nanorods arranged in a pseudo-cholesteric pattern. Microcompression pillar tests revealed a considerable failure strength over 3 GPa, which is higher than most natural materials. The investigated natural composite clearly shows the activation of micropolar rotation of the constituting phase and in-plane negative Poisson's ratio. Through DIC analysis, we confirm that the observed auxeticity can indeed be attributed to the rotation of nanorods during deformation driven by the modulus asymmetry between nanorods and matrix, as well as the anisotropic stiffness constants of goethite nanorods. The close association between auxeticity and microstructural rotation was further verified from linear elastic FEM analyses of the reconstructed microstructures, which reproduced the stiffness but could not reliably induce the rotation behavior and thus did not show auxeticity. Local particle rotations have also been found to result in auxeticity in nacre (*34*, *35*). The rotation mechanism observed in nacre is enabled by a "pushing-apart" interaction between neighboring grains, which requires a relatively high volume fraction of the stiff-phase material (aragonite) of about 95% (*36*). However, the nanorods in limpet teeth, in comparison to the aragonite plates in nacre, are much less densely packed with a volume fraction of around 51%. In the limpet teeth, two characteristic rotation modes, i.e., the revolving spin pattern of nanorods and their simultaneous on-axis rotation, constitute a highly unique spiraling microstructure that accommodates the loading and expands laterally. Key microstructural features leading to this behavior in limpet teeth include the pseudo-cholesteric arrangement of nanorods at appropriate volume fractions and aspect ratios, the anisotropic elasticity of nanorods with a goethite crystal structure that tends to align its compliant axis to the loading direction, and a nanometer-thick interfacial phase facilitating strong cohesion and effective stress transfer between nanorods and matrix. Theoretical and experimental studies (*15*, *37*–*39*) have shown that auxetic materials exhibit enhanced mechanical properties against compression loading, which is consistent with the primary mechanical function of limpet teeth (*20*). Therefore, the unique combination of auxeticity with extreme strength and high stiffness in the leading part of limpet teeth could be the primary reason for the superior resistance

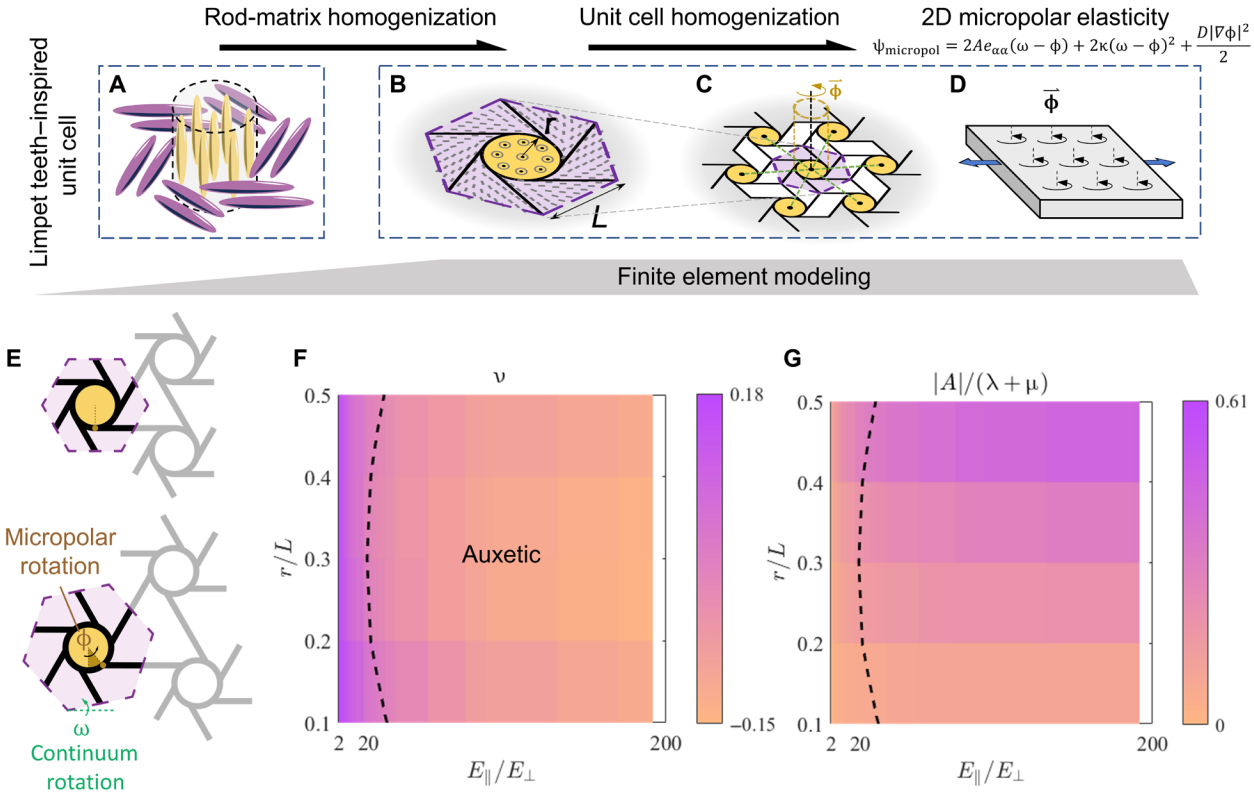

Fig. 5. Unit cell model accounting for microstructural rotation based on micropolar elasticity. (**A**) Vertical-horizontal nanorod bundle structure of limpet tooth taken as the basis of the unit cell model. (**B**) Inside the central node of the unit cell, the orientation is out of plane, while in the six adjacent arm domains, the orientation, denoted by short line segments, forms a revolving pattern. (**C**) A micropolar continuum constructed by assembling multiple unit cells. Here, the micropolar rotation ϕ in micropolar elasticity is defined as the mean rotation in the central node, while the continuum spin ω is defined as the average spin in the entire unit cell. (**D**) A micropolar elasticity part $\psi_{micropol}$ of the total strain energy density in a 2D form. Here, the total strain energy density consists of a conventional linear elasticity part with Lamé constants λ and μ (not shown) and $\psi_{micropol}$ as defined in the figure; $e_{\alpha\alpha}$ denotes the 2D areal strain, ω and ϕ are the continuum and the microscopic spin, respectively, while A, κ, and D are the material parameters. (**E**) Schematics of the deformation of a micropolar solid. The deformation is realized through the rotations of the microstructures, including the continuum spin (rigid body rotation) ω and the micropolar rotation ϕ (movie S8). (**F**) Poisson's ratio ν and (**G**) micropolarity, defined as $|A|/(\lambda+\mu)$, of the unit cell under different relative node size r/L and modulus anisotropy $E_{/\!/}/E_\perp$ ratios.

of limpet teeth against contact deformation and damage during harsh feeding conditions. Nevertheless, since biological materials vary broadly in their functionalities, not all of them need to evolve auxetic behavior. In general, the observed enhanced microstructure, especially the gradient interface that optimizes stress transfer between nanorods and matrix, can guide the design of biomimetic auxetic structures uniting high strength, high stiffness, and superior damage tolerance during contact.

MATERIALS AND METHODS

Transmission electron microscopy

The investigated radulae of limpet were extracted by dissection and cleaning using ethanol. Sampling for microstructure characterization and mechanical testing was conducted using only matured teeth. The samples for TEM characterization were prepared site-specifically using a FIB (JIB-4601F, JEOL, Japan). Two aberration-corrected STEM systems (JEM-ARM300CF and JEM-ARM200F, JEOL, Japan) were used for bright-field TEM, HRTEM, and STEM imaging, as well as EDS and EELS.

The in situ TEM tensile straining experiments were conducted using the STEM (JEM-ARM300CF, JEOL, Japan) operating at 300 kV using a single-tilt staining holder (model 654, Gatan). The TEM tensile straining samples were extracted by site-specific FIB lift-out and glued on a custom-made Cu straining grid by depositing Pt in a FIB. Real-time TEM movies were recorded using a charge-coupled device camera (OneView, Gatan, Pleasanton, USA) at 25 frames/s.

The tilt-series TEM tomography was conducted using the KBSI Bio-HVEM System (JEM-1000BEF, JEOL, Japan) operated at 1 MV. The TEM sample prepared by FIB was tilted from +50° to −50° with a tilting interval of 0.5°. In total, 201 tilt-series images were recorded and aligned by using a TEM recorder software (JEOL System Technology, Tokyo, Japan) and tomographically reconstructed using Composer and Visualizer-Kai software (TEMography.com, System in Frontiers Inc., Tokyo, Japan). Surface rendering and 3D modeling were performed using AMIRA software [Thermo Fisher Scientific (FEI), Hillsboro, USA].

DIC for strain and spin measurement and GPA analysis of in situ TEM images

In Fig. 4A and figs. S11 and S16, the open-source DIC package ncorr (*40*) was used to process the in situ TEM and STEM images obtained during tensile straining. The images before and after deformation were compared, and for each region from the before-deformation

image, the most correlated region on the after-deformation image was chosen to establish a displacement mapping ($u_z(\mathbf{x})$, $u_x(\mathbf{x})$) from which the strain field was computed. The maximum iteration number of the correlation process was set to 100 for all images. The software package was modified to calculate the spin around the out-of-plane axis, defined as $\omega_{zx} = \frac{1}{2}\left[\frac{\partial u_x}{\partial z} - \frac{\partial u_z}{\partial x}\right]$. The acquired strain fields $\epsilon_{zz}(\mathbf{x})$ and $\epsilon_{xx}(\mathbf{x})$ were averaged to obtain the mean $\overline{\epsilon}_{zz}$ and $\overline{\epsilon}_{xx}$, leading to the Poisson's ratio of the sample (here, z is the loading direction), $\nu = -\overline{\epsilon}_{xx}/\overline{\epsilon}_{zz}$. The spin pattern was further compared and correlated with the spatial pattern of the goethite nanorods.

GPA (HREM Research Inc., Japan) software was used for strain mapping of in situ HRTEM images. The HRTEM images were filtered by using a Wiener filter to remove the background noise. To apply the identical reference area for strain mapping, the HRTEM images taken at different displacements are stitched to a single image, where one taken at the smallest displacement served as a reference for strain mapping (refer to fig. S14A). The [100] direction of the goethite crystals is set to the x axis and of [010] to the y axis (fig. S14B). The lattice parameters of goethite with the orthorhombic crystal system (space group *Pbnm*) used in this study are a = 0.4598 nm, b = 0.9951 nm, and c = 0.3018 nm.

DIC for quantitative measurement of on-axis nanorod rotation

To measure the on-axis rotation direction and angle of each vertical nanorod in a bundle, the region of interest containing a single nanorod was selected and cropped from two TEM images taken before and after tensile straining (fig. S13). The contrast of each image was inverted to improve the detection efficiency of the nanorod edge. The image after straining was rotated stepwise by 0.1° in the range of −10° to 10° and shifted back to match the original nanorods by steps of 0.5 pixel along the x and y directions in the range of −5 to 5 pixels. The root mean square error (RMSE) was calculated for the rotated image correlating to the original image of the corresponding nanorod taken before straining. The rotation direction and angle were determined by finding the condition that yields the minimum RMSE, i.e., the best match between the two nanorod images. Although the diffraction contrast of nanorods changes during tensile straining, the contrast defining the nanorod edge, i.e., the intensity difference between the nanorod and matrix, remains sufficiently high, so it does not affect the reliability of edge detection. We assumed that the (projected) shape of the nanorod does not change significantly during tensile straining. This process was repeated for multiple vertical nanorods in a bundle. The results obtained from different vertical bundles within the same sample are shown in Fig. 4B and fig. S12D.

Microcompression experiments

For micropillar compression tests, individual mature teeth were cut from the radula using a scalpel and mounted in an upright position on silicon plates using epoxy resin as glue (see fig. S6A) under a stereo microscope. Subsequently, they were coated with a 10-nm-thick carbon layer to improve electrical conductivity to facilitate SEM observation and loaded in a FIB (Zeiss Auriga, Zeiss GmbH, Oberkochen, Germany) equipped with a femtosecond laser (Origami 10 XP, Onefive GmbH, Regensdorf, Switzerland) (*41*) to perform horizontal laser cuts on all prepared teeth, thus removing the tooth tip and exposing the specimen cross section. Additional laser cuts were performed to yield a lamella at the desired position for the samples, which was then also FIB-polished. Subsequently, pillars with rectangular-shaped cross sections were milled by FIB from this lamella (Fig. 3B). The micropillar cross sections were between 3 μm by 3μm and 5 μm by 5 μm and thus much larger compared to fiber bundles or their spacing. Microstructural features in the pillars (insets in fig. S6B) were clearly visible and enabled to identify whether samples were situated in the leading or trailing part, respectively.

Microcompression tests were performed in situ in a field-emission SEM (Zeiss LEO 982, Zeiss GmbH, Oberkochen, Germany) using an UNAT-SEM indenter (Zwick GmbH & Co. KG, Ulm, Germany) equipped with a conductive diamond flat punch indenter tip (19 μm in diameter; Synton-MDP AG, Nidau, Switzerland). Tests were performed at a constant displacement rate of 10 nm s^{-1}, corresponding to a nominal strain rate of 0.001 s^{-1}, and all pillars were loaded until failure. The raw load-displacement data were corrected for system compliance and converted to stress-strain curves using the initial pillar dimensions. Figure S6 (D and E) provides still images of the in situ video recorded during such an experiment at the beginning and during the experiment, respectively. Note that not only the pillar was deformed due to the indenter displacement δ_i but also the base of the pillar, and therefore, all material underneath it was displaced by δ_c due to nonzero system compliance. This was accounted for to measure the actual displacement and calculate the strain on the sample

$$\Delta L = L_2 - L_1 = \delta_i - \delta_c$$

$$\Delta\epsilon_{axial} = \frac{\Delta L}{L_1}$$

To analyze the Poisson's ratio, the change in width of the pillars Δw had to be measured. As Δw tended to be a relatively small quantity and given the 18.5-nm pixel resolution of the in situ SEM images necessary to cover the whole experiment, this proved to be challenging. To achieve a robust statistical measurement, each pillar was measured 10 times at around $\frac{L}{2}$ in unloaded and loaded states, respectively. The error of measurement for each independent evaluation was estimated to be 1 pixel. The Poisson's ratio ν of each pillar was subsequently calculated using

$$\nu = -\frac{\Delta\epsilon_{trans}}{\Delta\epsilon_{axial}} = -\frac{\frac{\Delta w}{w_1}}{\frac{\Delta L}{L_1}}$$

Microstructure reconstruction via FIB serial sectioning

Serial sectioning SEM imaging of limpet teeth was conducted by using a FIB (Zeiss, Crossbeam 550, Germany) at an image resolution of 2048 × 1536 pixels, scan speed of 46.8 s, and magnification of 20,100. Samples for FIB serial sectioning were prepared by depositing a ~4-nm-thick Pt conducting layer to avoid charging effects. Carbon tape and silver paste were used to fix the specimen on the FIB holder. At the regions of interest, a ~1-mm-thick Pt protection layer was deposited. FIB milling was performed using Ga^+ ions at 30 kV. SEM images were acquired after milling the region of interest by an average thickness of 7 nm for each milling section (pixel size of 2.8 nm). To reduce curtaining effects caused by the Ga^+ ion beam, fine milling was performed using a beam current of 100 pA after rough milling with a beam current of 20 nA.

The microstructure reconstruction for FE analyses has been carried out using a set of the serial-sectioned SEM images of the leading part. The applied image processing steps using the open-source image analysis platform Fiji (*42*) include background subtraction, bandpass filtering, drift/tilt correction, image cropping, Gaussian blurring

(for unspeckled binary image generation), local thresholding (to create binary images), and scaling/coarsening (scaling and reduction of in-plane resolution for isotropic voxel sizes in 3D and computationally manageable voxel-based FE models). Morphological operators of opening, closing, dilating, and eroding were used if necessary. Last, a MATLAB code was written to convert the binarized image sequence to voxel-based Abaqus FE models. The FE schemes used in the analyses were four-node bilinear plane-stress (CPS4) and plane-strain (CPE4) elements for 2D models and eight-node linear hexahedral solid elements with reduced integration (C3D8R) for 3D models.

FEM of a unit cell

The goethite-hydrated silica composite was locally homogenized as an orthotropic material with in-plane isotropy, and therefore, one material orientation needed to be specified. Homogenization using the Mori-Tanaka theory requires the input of elastic material constants of both phases, λ_{rod}, μ_{rod} and λ_{mat}, μ_{mat}, together with the effective rod aspect ratio and the volume fraction f of the goethite nanorods. First, with Eshelby's transformation tensor S_{ijkl}, the following dimensionless constants (*31*, *32*) were defined

$$D_1 = 1 + 2[\mu_{rod} - \mu_{mat}]/[\lambda_{rod} - \lambda_{mat}]$$

$$D_2 = [\lambda_{mat} + 2\mu_{mat}]/[\lambda_{rod} - \lambda_{mat}]$$

$$D_3 = \lambda_{mat}/[\lambda_{rod} - \lambda_{mat}]$$

$$B_1 = fD_1 + D_2 + [1 - f][D_1 S_{1111} + 2S_{2211}]$$

$$B_2 = f + D_3 + [1 - f][D_1 S_{1122} + S_{2222} + S_{2233}]$$

$$B_3 = f + D_3 + [1 - f][S_{1111} + [1 + D_1]S_{2211}]$$

$$B_4 = fD_1 + D_2 + [1 - f][S_{1122} + D_1 S_{2222} + S_{2233}]$$

$$B_5 = f + D_3 + [1 - f][S_{1122} + S_{2222} + D_1 S_{2233}]$$

$$A_1 = D_1[B_4 + B_5] - 2B_2$$

$$A_2 = [1 + D_1]B_2 - [B_4 + B_5]$$

$$A_3 = B_1 - D_1 B_3$$

$$A_4 = [1 + D_1]B_1 - 2B_3$$

$$A_5 = [1 - D_1]/[B_4 - B_5]$$

$$A^* = 2B_2 B_3 - B_1[B_4 + B_5]$$

The longitudinal Young's modulus of the homogenized composite can be written as

$$\frac{E_\parallel}{E_{mat}} = \frac{E_l}{E_{mat}} = \frac{1}{1 + f[A_1 + 2\nu_{mat}A_2]/A^*}$$

while the transverse Young's modulus of the homogenized composite is equal to

$$\frac{E_\perp}{E_{mat}} = \frac{E_t}{E_{mat}} = \frac{1}{1 + f[-2\nu_{mat}A_3 + (1 - \nu_{mat})A_4 + (1 + \nu_{mat})A_5 A^*]/2A^*}$$

The in-plane shear modulus takes the form

$$\frac{\mu_{lt}}{\mu_{mat}} = 1 + \frac{f}{\frac{\mu_{mat}}{\mu_{rod} - \mu_{mat}} + 2[1 - f]S_{1212}}$$

and the out-of-plane shear modulus is

$$\frac{\mu_t}{\mu_{mat}} = 1 + \frac{f}{\frac{\mu_{mat}}{\mu_{rod} - \mu_{mat}} + 2[1 - f]S_{2323}}$$

Last, the major Poisson's ratio of the composite reads (*43*)

$$\nu_{lt} = \frac{\nu_{mat}A^* - f(A_3 - \nu_{mat}A_4)}{A^* + f(A_1 + 2\nu_{mat}A_2)}$$

Inspired by the nanorod-matrix distribution pattern observed in TEM images, the representative orientation pattern on a hexagon was constructed to obtain macroscopic isotropy, as shown in Fig. 5 (A and B), with a central circular node with radius r and an out-of-plane orientation resembling the vertical bundle. Surrounding it were the six arm domains wherein the orientations were mainly aligned toward one direction in each domain, in line with the horizontal bundle. The orientation pattern near the domain boundaries was smoothened to avoid any orientation discontinuity across domains. Together, these domains formed a spiral-like structure revolving around the central node. Periodic boundary conditions upon all diagonal side pairs on the hexagon were applied, and the model was subjected to various loadings, including uniaxial and biaxial tension, shear, and body moment under the plane-strain condition to characterize its micropolar elastic constants (see the next section). It was also subjected to uniaxial tension under plane-stress condition, similar to the experiments, to characterize its Poisson's ratio ν.

Micropolar elasticity modeling characterization

Among various continuum mechanics theories, linear elasticity assumes both infinitesimal strain and infinitesimal rotation and that the rotation part does not contribute to the strain energy of the material. To account for the observed significant rotation, micropolar elasticity was considered, where a microscopic rotation is introduced to account for the rotational deformation of the microstructure. Both macroscopic strain and microscopic rotation can induce stress, and the latter can lead to a couple stress as well. Here, the 2D scenario was considered, where the constitutive relation for the stress can be written as (*44*)

$$\begin{bmatrix}\sigma_{11}\\ \sigma_{22}\\ \sigma_{12}\\ \sigma_{21}\end{bmatrix} = \begin{bmatrix}2\mu + \lambda & \lambda & -A & A\\ \lambda & 2\mu + \lambda & -A & A\\ A & -A & \mu + \kappa & \mu - \kappa\\ A & -A & \mu - \kappa & \mu + \kappa\end{bmatrix}\begin{bmatrix}u_{1,1}\\ u_{2,2}\\ u_{2,1} - \phi\\ u_{1,2} + \phi\end{bmatrix}$$

with $u_{i,j}$ being the displacement gradient, σ_{ij} the stress, and ϕ the microscopic spin around the out-of-plane axis. The stress tensor may no longer be symmetric ($\sigma_{12} \neq \sigma_{21}$) as a body moment can exist. The constitutive relation for the couple stress was not included here, which is related to the gradient of the microscopic spin ϕ. Apart from the classical Lamé constants (λ and μ), additional parameters (A and κ) were needed. We restricted ourselves to $|A|$, as the sign of A represents the chirality of the structure, which was not of interest in this study.

To characterize these parameters, the structure was first put under uniaxial tension, biaxial tension, and shear loading. Then, the area of the element was fixed while rotating the central node. Therefore, a body moment was introduced. The last loading condition was necessary to trigger the micropolar elastic mode of deformation. Nevertheless, in a larger lattice of the proposed unit cell, the micropolar elastic deformation can be triggered by a heterogeneous distribution of strain and stress as well. Among all loading conditions, the area-averaged spin around the out-of-plane axis inside the central node was treated as the microscopic spin ϕ, while the average displacement gradient and stress inside the entire model were regarded as $u_{i,j}$ and σ_{ij}. Next, we write down the constitutive relations for all loadings with (λ, μ, A, κ) as variables and solve the equations with a least-square error.

SUPPLEMENTARY MATERIALS

Supplementary material for this article is available at https://science.org/doi/10.1126/sciadv.add4644

REFERENCES AND NOTES

1. M. A. Meyers, J. McKittrick, P.-Y. Chen, Structural biological materials: Critical mechanics-materials connections. *Science* **339**, 773–779 (2013).
2. U. G. K. Wegst, H. Bai, E. Saiz, A. P. Tomsia, R. O. Ritchie, Bioinspired structural materials. *Nat. Mater.* **14**, 23–36 (2015).
3. J. Wilmers, S. Bargmann, Nature's design solutions in dental enamel: Uniting high strength and extreme damage resistance. *Acta Biomater.* **107**, 1–24 (2020).
4. C. Ortiz, M. C. Boyce, Bioinspired structural materials. *Science* **319**, 1053–1054 (2008).
5. J. W. Pro, F. Barthelat, The fracture mechanics of biological and bioinspired materials. *MRS Bulletin* **44**, 46–52 (2019).
6. J. L. Williams, J. L. Lewis, Properties and an anisotropic model of cancellous bone from the proximal tibial epiphysis. *J. Biomech. Eng.* **104**, 50–56 (1982).
7. R. Gatt, M. Vella Wood, A. Gatt, F. Zarb, C. Formosa, K. M. Azzopardi, A. Casha, T. P. Agius, P. Schembri-Wismayer, L. Attard, N. Chockalingam, J. N. Grima, Negative Poisson's ratios in tendons: An unexpected mechanical response. *Acta Biomater.* **24**, 201–208 (2015).
8. D. R. Veronda, R. A. Westmann, Mechanical characterization of skin—Finite deformations. *J. Biomech.* **3**, 111–122 (1970).
9. C. Lees, J. F. V. Vincent, J. E. Hillerton, Poisson's ratio in skin. *Biomed. Mater. Eng.* **1**, 19–23 (1991).
10. F. Song, J. Zhou, X. Xu, Y. Xu, Y. Bai, Effect of a negative Poisson ratio in the tension of ceramics. *Phys. Rev. Lett.* **100**, 245502 (2008).
11. K. J. Koski, P. Akhenblit, K. McKiernan, J. L. Yarger, Non-invasive determination of the complete elastic moduli of spider silks. *Nat. Mater.* **12**, 262–267 (2013).
12. K. E. Evans, M. A. Nkansah, I. J. Hutchinson, S. C. Rogers, Molecular network design. *Nature* **353**, 124 (1991).
13. R. Lakes, Deformation mechanisms in negative Poisson's ratio materials: Structural aspects. *J. Mater. Sci.* **26**, 2287–2292 (1991).
14. R. Lakes, Advances in negative Poisson's ratio materials. *Adv. Mater.* **5**, 293–296 (1993).
15. K. E. Evans, A. Alderson, Auxetic materials: Functional materials and structures from lateral thinking! *Adv. Mater.* **12**, 617–628 (2000).
16. C. Huang, L. Chen, Negative poisson's ratio in modern functional materials. *Adv. Mater.* **28**, 8079–8096 (2016).
17. P. Van der Wal, H. J. Giesen, J. J. Videler, Radular teeth as models for the improvement of industrial cutting devices. *Mater. Sci. Eng. C* **7**, 129–142 (1999).
18. D. Lu, A. H. Barber, Optimized nanoscale composite behaviour in limpet teeth. *J. R. Soc. Interface* **9**, 1318–1324 (2012).
19. A. H. Barber, D. Lu, N. M. Pugno, Extreme strength observed in limpet teeth. *J. R. Soc. Interface* **12**, 20141326 (2015).
20. T. Ukmar-Godec, G. Kapun, P. Zaslansky, D. Faivre, The giant keyhole limpet radular teeth: A naturally-grown harvest machine. *J. Struct. Biol.* **192**, 392–402 (2015).
21. S. Keten, Z. Xu, B. Ihle, M. J. Buehler, Nanoconfinement controls stiffness, strength and mechanical toughness of β-sheet crystals in silk. *Nat. Mater.* **9**, 359–367 (2010).
22. P. Van der Wal, Structural and material design of mature mineralized radula teeth of *Patella vulgata* (gastropoda). *J. Ultrastruct. Mol. Struct. Res.* **102**, 147–161 (1989).
23. E. D. Sone, S. Weiner, L. Addadi, Morphology of goethite crystals in developing limpet teeth: Assessing biological control over mineral formation. *Cryst. Growth Des.* **5**, 2131–2138 (2005).
24. H. Gao, B. Ji, I. L. Jäger, E. Arzt, P. Fratzl, Materials become insensitive to flaws at nanoscale: Lessons from nature. *Proc. Natl. Acad. Sci. U.S.A.* **100**, 5597–5600 (2003).
25. S.-Y. Chen, A. Gloter, A. Zobelli, L. Wang, C.-H. Chen, C. Colliex, Electron energy loss spectroscopy andab initioinvestigation of iron oxide nanomaterials grown by a hydrothermal process. *Phys. Rev. B* **79**, 104103 (2009).
26. C. H. Chang, C. H. Hsieh, J. C. Huang, C. Wang, Y. C. Liao, C. H. Hsueh, X. H. du, Z. K. Wang, X. Wang, Designing a stronger interface through graded structures in amorphous/nanocrystalline ZrCu/Cu multilayered films. *Nanotechnology* **27**, 225701 (2016).
27. S. Suresh, Graded materials for resistance to contact deformation and damage. *Science* **292**, 2447–2451 (2001).
28. L. M. Gordon, D. Joester, Nanoscale chemical tomography of buried organic–inorganic interfaces in the chiton tooth. *Nature* **469**, 194–197 (2011).
29. B. Ji, A study of the interface strength between protein and mineral in biological materials. *J. Biomech.* **41**, 259–266 (2008).
30. F. Song, A. K. Soh, Y. L. Bai, Structural and mechanical properties of the organic matrix layers of nacre. *Biomaterials* **24**, 3623–3631 (2003).
31. G. P. Tandon, G. J. Weng, The effect of aspect ratio of inclusions on the elastic properties of unidirectionally aligned composites. *Polym. Compos.* **5**, 327–333 (1984).
32. T. Mori, K. Tanaka, Average stress in matrix and average elastic energy of materials with misfitting inclusions. *Acta Metall. Mater.* **21**, 571–574 (1973).
33. A. B. Rinkevich, D. V. Perov, M. I. Samoilovich, S. M. Kleshcheva, Elastic properties and heat capacity of opal matrices and related 3D-nanocomposite materials. *Solid State Phys.* **52**, 2570–2576 (2010).
34. X. Li, Z.-H. Xu, R. Wang, In situ observation of nanograin rotation and deformation in nacre. *Nano Lett.* **6**, 2301–2304 (2006).
35. W. Yang, Z. Gao, Z. Yue, X. Li, B. Xu, Hard-particle rotation enabled soft–hard integrated auxetic mechanical metamaterials. *Proc. R. Soc. A* **475**, 20190234 (2019).
36. N. Watabe, K. M. Wilbur, Eds., Mechanisms of mineralization in the invertebrates and plants, in *International Symposium on the Mechanisms of Mineralization in the Invertebrates and Plants* (University of South Carolina Press, Columbia, SC, 1976).
37. N. Chan, K. Evans, Indentation resilience of conventional and auxetic foams. *J. Cell. Plast.* **34**, 231–260 (1998).
38. I. I. Argatov, R. Guinovart-Díaz, F. J. Sabina, On local indentation and impact compliance of isotropic auxetic materials from the continuum mechanics viewpoint. *Int. J. Eng. Sci.* **54**, 42–57 (2012).
39. T. Li, F. Liu, L. Wang, Enhancing indentation and impact resistance in auxetic composite materials. *Compos. Part B Eng.* **198**, 108229 (2020).
40. J. Blaber, B. Adair, A. Antoniou, Ncorr: Open-source 2D digital image correlation Matlab software. *Exp. Mech.* **55**, 1105–1122 (2015).
41. M. J. Pfeifenberger, M. Mangang, S. Wurster, J. Reiser, A. Hohenwarter, W. Pfleging, D. Kiener, R. Pippan, The use of femtosecond laser ablation as a novel tool for rapid micro-mechanical sample preparation. *Mater. Des.* **121**, 109–118 (2017).
42. J. Schindelin, I. Arganda-Carreras, E. Frise, V. Kaynig, M. Longair, T. Pietzsch, S. Preibisch, C. Rueden, S. Saalfeld, B. Schmid, J.-Y. Tinevez, D. J. White, V. Hartenstein, K. Eliceiri, P. Tomancak, A. Cardona, Fiji: An open-source platform for biological-image analysis. *Nat. Methods* **9**, 676–682 (2012).
43. C. L. Tucker, E. Liang, Stiffness predictions for unidirectional short-fiber composites: Review and evaluation. *Compos. Sci. Technol.* **59**, 655–671 (1999).
44. X. N. Liu, G. L. Huang, G. K. Hu, Chiral effect in plane isotropic micropolar elasticity and its application to chiral lattices. *J. Mech. Phys. Solids* **60**, 1907–1921 (2012).
45. C. A. Schneider, W. S. Rasband, K. W. Eliceiri, NIH Image to ImageJ: 25 years of image analysis. *Nat. Methods* **9**, 671–675 (2012).
46. D. Tunega, Theoretical study of properties of goethite (α-FeOOH) at ambient and high-pressure conditions. *J. Phys. Chem. C* **116**, 6703–6713 (2012).

Acknowledgments: S.H.O. acknowledges the initial efforts of the team project members at SKKU. Y.L. acknowledges helpful discussions with B. Ni of Brown University. **Funding:** This work was supported by the National Research Foundation of Korea (NRF) grant NRF-2020R1A2C2101735, NRF-2019M3D1A1078299, and NRF-2018M3C1B7021994 (to S.H.O.), KENTECH Research Grant KRG2022-01-019 (to S.H.O.), German Research Foundation (DFG) grant 192346071 - SFB 986 (to S.B., X.-L.P., C.S., and J.W.), NSF grant CMMI-1562904 (to H.G. and Y.L.), and European Research Council (ERC) grant 771146 TOUGHIT (to D.K. and M.W.).
Author contributions: Conceptualization: S.H.O. and H.G. Methodology (TEM): Jiwon Jeong, J.S., Z.W., J.-K.K., Jeehun Jeong, S.H.O., H.-J.K., Y.H.H., and B.K. Methodology (microcompression): M.W. and D.K. Methodology (modeling): Y.L., H.G., X.-L.P., J.W., C.S., and S.B. Investigation (GPA and DIC): J.S., J.-K.K., J.K., Y.L., and S.H.O. Visualization (movies): Jiwon Jeong, H.-J.K., Y.H.H., S.H.O., X.-L.P., J.W., C.S., S.B., and Y.L. Funding acquisition: S.H.O., S.B., D.K., and H.G. Project administration: S.H.O. Supervision: S.H.O., S.B., D.K., and H.G. Writing—original draft: J.-K.K., Y.L., S.H.O., S.B., D.K., and H.G. Writing—review and editing: J.-K.K., M.W., D.K., X.-L.P., J.W., C.S., S.B., Y.L., H.G., and S.H.O. **Competing interests:** The authors declare that they have no competing interests. **Data and materials availability:** All data needed to evaluate the conclusions in the paper are present in the paper and/or the Supplementary Materials.

Submitted 14 June 2022
Accepted 19 October 2022
Published 2 December 2022
10.1126/sciadv.add4644

ScienceAdvances

Limpet teeth microstructure unites auxeticity with extreme strength and high stiffness

Sang Ho OhJin-Kyung KimYue LiuMichael WurmshuberXiang-Long PengJinsol SeoJiwon JeongZhen WangJana WilmersCelal SoyarslanJongil KimBoonsita KittiwirayanonJeehun JeongHyo-Jeong KimYang Hoon HuhDaniel KienerSwantje BargmannHuajian Gao

Sci. Adv., 8 (48), eadd4644. • DOI: 10.1126/sciadv.add4644

Science Advances (ISSN) is published by the American Association for the Advancement of Science. 1200 New York Avenue NW, Washington, DC 20005. The title *Science Advances* is a registered trademark of AAAS.